

Computations of the drag coefficients for low-Reynolds-number flow past rings

By G. J. SHEARD†, K. HOURIGAN AND M. C. THOMPSON

Fluids Laboratory for Aeronautical and Industrial Research (FLAIR), Department of Mechanical Engineering, Monash University, Melbourne, Victoria 3800, Australia

(Received 11 February 2004 and in revised form 14 October 2004)

The variation in the drag coefficient for low-Reynolds-number flow past rings orientated normal to the direction of flow is investigated numerically. An aspect ratio parameter is used for a ring, which describes at its limits a sphere and a circular cylinder. This enables a continuous range of bodies between a sphere and a circular cylinder to be studied.

The computed drag coefficients for the flow past rings at the minimum and maximum aspect ratio limits are compared with the measured and computed drag coefficients reported for the sphere and the circular cylinder. Some interesting features of the behaviour of the drag coefficients with variation of Reynolds number and aspect ratio emerge from the study. These include the decrease in the aspect ratio at which the minimum drag coefficient occurs as the Reynolds number is increased, from $A_R \approx 5$ at $Re = 1$ to $A_R \approx 1$ at $Re = 200$. In addition, a substantial decrease in the pressure component of the drag coefficient is observed after the onset of three-dimensional flow while the viscous contribution is similar to that for flow with imposed axisymmetry. Typically, the sudden reduction in drag caused by transition to Mode A shedding is 6%, which is consistent with the behaviour for flow past a circular cylinder. Power-law fits to the drag coefficient for $Re \lesssim 100$ are provided, which are accurate within approximately 2%.

1. Introduction

This paper reports on numerical computations of the drag imparted on a ring by flow normal to the plane of the ring. The present computations follow on from an earlier series of studies that investigated the flow past a ring at low Reynolds number. In Sheard, Thompson & Hourigan (2003) the stability of axisymmetric flow past rings was reported, and in Sheard, Thompson & Hourigan (2004*b*) the wake structure and nonlinear properties of these flows were examined using a Landau model. In this paper, the drag of rings has been quantified through a comprehensive and detailed numerical study in flows up to $Re \approx 350$.

The ring geometry is described by the aspect ratio parameter A_R , which is defined as the ratio of the mean ring diameter D to the cross-section diameter d . A sphere is therefore a ring with an aspect ratio $A_R = 0$, and the ring cross-section approaches a straight circular cylinder as $A_R \rightarrow \infty$. The Reynolds number is based on the length

† Author to whom correspondence should be addressed: Greg.Sheard@eng.monash.edu.au

Transition	Reynolds number
Boundary layer separation	21
Regular asymmetric transition – Regular bifurcation	211
Hopf transition – Hopf bifurcation	272

TABLE 1. Transitions in the flow past a sphere at low Reynolds number. The separation transition has been reported by Taneda (1956a), Johnson & Patel (1999) and Tomboulides & Orszag (2000) and the non-axisymmetric transitions have been investigated by Natarajan & Acrivos (1993), Johnson & Patel (1999), Tomboulides & Orszag (2000), Ghidersa & Dušek (2000) and Thompson *et al.* (2001).

scale d , so that

$$Re = \frac{U_\infty d}{\nu}, \quad (1.1)$$

where U_∞ is the free-stream velocity and ν is the kinematic viscosity of the fluid.

As the Reynolds number is increased from low values, the flow past bluff bodies undergoes a series of transitions. For bodies such as a sphere or a circular cylinder, the flow develops from steady attached creeping flow at the low-Reynolds-number limit (Taneda 1956a, b), to unsteady three-dimensional flow as the Reynolds number increases to $Re \approx 300$ for a sphere and $Re \approx 190$ for a circular cylinder (Achenbach 1974; Johnson & Patel 1999; Tomboulides & Orszag 2000; Williamson 1988b, 1996b). The low-Reynolds-number flow past a sphere and a circular cylinder has been widely studied, and is well understood. For the flow past these bodies, a substantial change in the drag coefficient occurs over the Reynolds number range $0 < Re \lesssim 350$, from a drag coefficient dominated by viscous forces at low Reynolds numbers, to a drag coefficient dominated by pressure forces at higher Reynolds numbers. The variation of drag coefficient with Reynolds number for a circular cylinder is given in Williamson & Roshko (1990) and Henderson (1995).

An understanding of the low-Reynolds-number flow past bluff bodies, and the dependence of properties such as the drag coefficient on alterations in body geometry, are important for a wide range of applications. For instance, an interest in sedimentation and microbiological flows fuelled attempts to analytically describe the creeping flow past open rings by Johnson & Wu (1979) and Goren & O'Neill (1980). For Reynolds numbers beyond the high-Reynolds-number limit of the present study ($Re \gtrsim 350$), studies have shown that for the flow past spheres (Johnson & Patel 1999; Tomboulides & Orszag 2000) and circular cylinders (Henderson 1995, 1997), little variation in the drag coefficient is observed with an increase in the Reynolds number until boundary-layer transition is encountered at Reynolds numbers of $O(10^5)$. The Reynolds number range $0 < Re \lesssim 350$ defines a regime of great change in both the drag coefficient and the physical structure of the flow past bluff bodies in general, and in particular, the flows past the rings, spheres and circular cylinders considered in this study. Tables 1 and 2 list the transitions in the wake of a sphere and a circular cylinder, respectively, over the relevant Reynolds number range.

For the flow past a sphere, the drag coefficient decreases with an increase in Reynolds number from $Re \approx 0$ to $Re \approx 300$. The observed decrease in C_D is caused by a decrease in the viscous component of the drag coefficient with increasing Reynolds number. For a cylinder, the behaviour varies depending on whether the flow is steady or unsteady. When the flow is steady ($0 < Re \lesssim 47$), both the pressure and viscous components of the drag coefficient decrease with an increase in the Reynolds number

Transition	Reynolds number
Boundary layer separation	5
Hopf transition – Hopf bifurcation	47
Three-dimensional transition – Hopf bifurcation	188.5

TABLE 2. Transitions in the flow past a circular cylinder. The flow separation transition was reported by Taneda (1956*b*) and Noack & Eckelmann (1994), the Hopf bifurcation by Provansal *et al.* (1987), Williamson (1988*a*), Dušek *et al.* (1994) and Williamson (1996*b*), and the three-dimensional transition by Williamson (1988*b*), Thompson, Hourigan & Sheridan (1994, 1996), Barkley & Henderson (1996) and Henderson (1997).

(Henderson 1995). For unsteady flow ($Re \gtrsim 47$), the pressure component of the drag coefficient increases with an increase in Reynolds number, and at $Re \approx 150$, this increase offsets the decrease in the viscous component.

No previous studies have reported the low-Reynolds-number drag coefficients of the flow past rings. Experimental studies of the flow past rings by Roshko (1954), Monson (1983), Bearman & Takamoto (1988) and Leweke & Provansal (1995) have all observed that at large aspect ratios, the flow is locally similar to the flow past a circular cylinder, and at small aspect ratios the flow is similar to the flow past a sphere. These studies proposed that the critical aspect ratio for the transition between these flow regimes was in the range $4 \lesssim A_R \lesssim 7$. The detailed computations of Sheard *et al.* (2003, 2004*b*) refined this value to $A_R \approx 3.9$. In figure 1, streamline plots of the steady or time-averaged flows past a sphere, a sequence of rings with aspect ratios $1 \leq A_R \leq 5$, and a circular cylinder are presented. Notice that with an increase in aspect ratio, the wake structure transforms from one similar to the flow past a sphere (figure 1*a*) to the flow past a circular cylinder (figure 1*f*). Figure 1(*b*) shows a modified body geometry that was employed to overcome singularities where the ring cross-sections meet the symmetry axis at $A_R = 1$. This treatment is discussed in detail in Sheard (2004), where it is shown that the minor modification had an insignificant effect on the surrounding flow and transitions. This paper presents, for the first time, a systematic study of the relationship of the drag coefficient with aspect ratio and Reynolds number for rings.

2. Methodology

In this section, the numerical technique employed to compute the flow is described, together with details of how the drag coefficients were evaluated.

2.1. Flow computations with the spectral-element method

The computations in the present investigation were performed using a spectral-element method. In a previous study (Thompson, Leweke & Provansal 2001) it was successfully applied to compute the flow past a sphere. The method has also been applied to compute the axisymmetric and non-axisymmetric flows past rings in studies by Sheard *et al.* (2003) and Sheard *et al.* (2004*a, b*), respectively.

The spectral-element method as applied in this study employed a weighted-residual technique for spatial discretization of the Navier–Stokes equations, and for temporal integration of the flow, a three-step splitting scheme was used (e.g. see Patera 1984; Tomboulides & Orszag 2000). The meshes comprised quadrilateral elements, and Gauss–Lobatto–Legendre quadrature was used to integrate over the elements. The functional variation of flow variables within elements was represented by Lagrangian

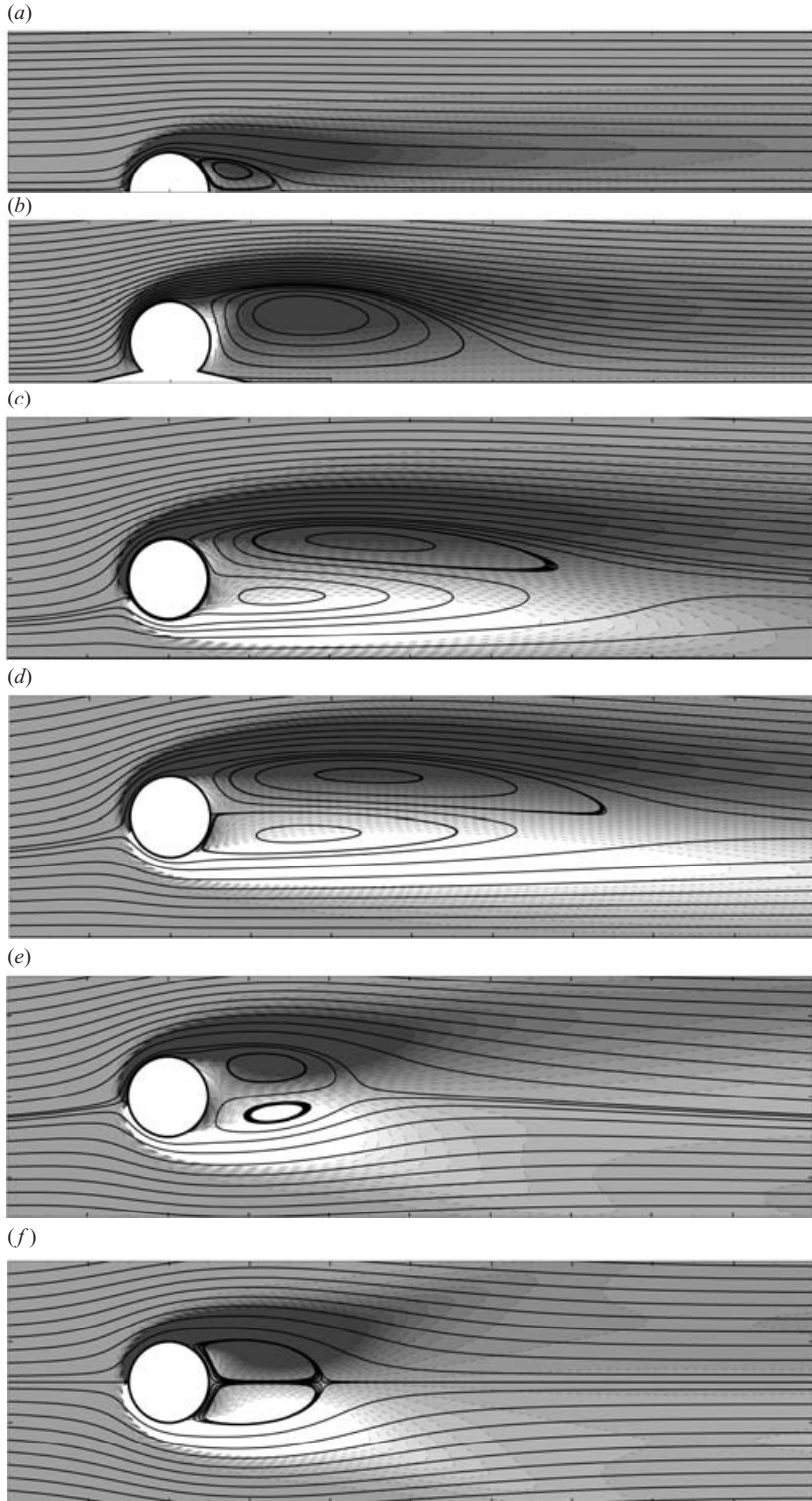


FIGURE 1. For caption see facing page.

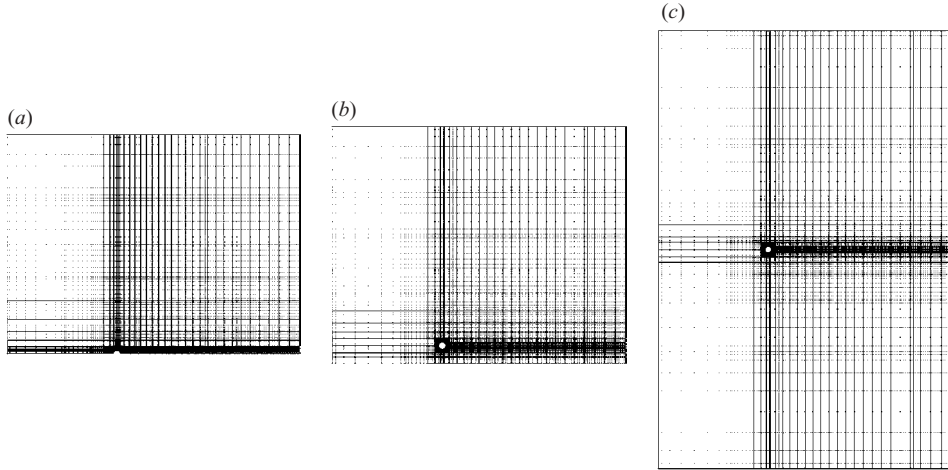


FIGURE 2. The meshes employed to model the flow past rings with $A_R = 0$ (a), $A_R = 5$ (b), and a circular cylinder (c). Sub-elements are shown, and flow is computed from left to right; for axisymmetric meshes, a zero, normal-velocity condition is imposed at the axis at the bottom of the meshes. On the upstream and transverse boundaries, a uniform free-stream velocity condition is imposed, on the downstream boundary a zero gradient of velocity is imposed, and on the circular ring cross-section, a zero velocity boundary is imposed.

tensor-product polynomials, with internal node points that corresponded to the Gauss–Legendre–Lobatto collocation points. For the ring computations, the spectral-element mesh was used to discretize the flow in the z – r plane (and the x – y plane for the circular cylinder) around the circular ring cross-section. A normal velocity condition was enforced at the downstream boundary, and for transverse and upstream boundaries a uniform free-stream velocity condition was employed.

For mesh consistency for different aspect ratios, the computational domain away from the axis did not vary with aspect ratio. The distance between the ring cross-section and the geometrical axis of symmetry was varied to treat the different aspect ratios considered. For further details see Sheard *et al.* (2003, 2004b) and Sheard (2004). The meshes employed in the study consisted of between 380 and 420 macro-elements with a polynomial order of $N^2 = 81$. To minimize blockage effects, a transverse domain size of $30d$ was employed, and the domain extended $15d$ upstream and $25d$ downstream of the ring cross-section. Grid independence studies (Sheard 2004) verified that the meshes led to solutions accurate to within approximately 1% up to $Re = 350$. Figure 2 shows examples of the set of meshes employed to model the flows in this study.

For non-axisymmetric computations, a Fourier expansion of the velocity and pressure fields in the azimuthal direction was employed. Similar to the approach taken by Tomboulides, Orszag & Karniadakis (1993) and Tomboulides & Orszag

FIGURE 1. Streamline plots of the steady and time-averaged flows past a sphere (a), rings with aspect ratios $A_R = 1$ (b), $A_R = 2$ (c), $A_R = 3$ (d) and $A_R = 5$ (e), and a circular cylinder (f) at $Re = 100$. Vorticity is shown by dotted lines and contours, with negative and positive vorticity shaded dark and light, respectively. Contour and streamline levels are arbitrary, and flow is from left to right. In (a–d), the symmetry axis is at the bottom of each frame. In (e), the frame is localized to the cross-section of the ring away from the axis, and in (f), no symmetry axis exists as the computation was two-dimensional.

(2000), the present formulation of the method has been successfully applied to model the non-axisymmetric flow past a sphere by Thompson *et al.* (2001), and rings by Sheard *et al.* (2004a, b).

2.2. Calculation of the drag coefficient

The drag coefficient may be defined as

$$C_D = \frac{F_D}{\frac{1}{2}\rho A_{frontal} U_\infty^2}, \quad (2.1)$$

where ρ , $A_{frontal}$ and U_∞ are the fluid density, the projected frontal area of the body, and the free-stream velocity of the fluid, respectively.

The frontal area $A_{frontal}$ can be reduced to a function of A_R when dimensions are scaled by d . This allows the drag coefficient to be evaluated from

$$\rho U_\infty^2 C_D = \begin{cases} \frac{F_D}{\frac{1}{2}\pi(A_R^2 + 2A_R + 1)} = \frac{8F_D}{\pi(A_R^2 + 2A_R + 1)} & \text{for } 0 \leq A_R \leq 1, \\ \frac{F_D}{\frac{1}{2}\pi A_R} = \frac{2F_D}{\pi A_R} & \text{for } A_R > 1. \end{cases} \quad (2.2)$$

The drag force comprises a pressure component and a viscous component, i.e. $F_D = F_{D_p} + F_{D_v}$. The methods used to compute the force components are similar to those described variously in Blackburn & Henderson (1994, 1996), Henderson (1995) and Jenny, Dušek & Bouchet (2004).

3. Comparisons with previous studies

In this section, the drag coefficients are computed for a sphere and a circular cylinder. The predictions are compared to previous experimental measurements and computations of the drag, in order to validate the present numerical method and implementation.

3.1. Drag coefficients computed for the flow past a sphere

A plot of the computed drag coefficients for the axisymmetric flow past a sphere is presented in figure 3. The plot shows that the present predictions are generally within 1% of previous measurements and computations. Notice that the transition to non-axisymmetric and unsteady flows does not abruptly alter the shape of the curve. This is not surprising, as Ghidersa & Dušek (2000) and Thompson *et al.* (2001) show that both of these transitions occur through continuous bifurcations.

3.2. Drag coefficients computed for the flow past a circular cylinder

A plot of the computed drag coefficients for the two-dimensional flow past a circular cylinder is presented in figure 4. The plot shows that the present predicted coefficients were generally within 10% of previous measurements and computations. Importantly, throughout the steady and unsteady two-dimensional flow regimes, the computed drag coefficients lie close to the mean of the previous experimental measurements. The reason for the greater scatter of the data observed in figure 4 when compared with figure 3 is due to the influence of end-effects on the measurements. The flow conditions in the vicinity of the cylinder ends are generally far from two-dimensional and can cause non-parallel wake patterns. The effect of the end-conditions in experimental studies of the flow past a circular cylinder has been considered in a number of studies,

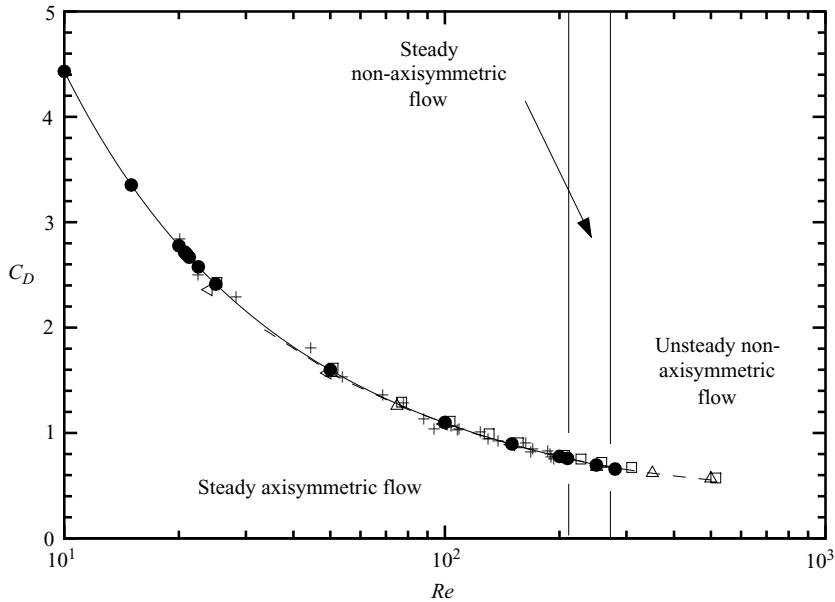


FIGURE 3. A comparison between the computed drag coefficients for the flow past a sphere (solid line and circles) with previously reported values. The dashed line shows the curve determined by an experimental collocation by Clift, Grace & Weber (1978), and + represents the experimental measurements of Roos & Willmarth (1971). The symbols \square , \triangle and \triangleleft represent the drag coefficients computed by Tomboulides, Orszag & Karniadakis (1993), Mittal (1999) and Johnson & Patel (1999), respectively. The vertical lines indicate the Reynolds numbers for the transition from axisymmetric to non-axisymmetric flow at $Re \approx 210$, and the transition from steady to unsteady flow at $Re \approx 272$.

which include Williamson (1989, 1992), Norberg (1994), Leweke & Provansal (1995) and Williamson (1996c).

At Reynolds numbers beyond the critical Reynolds number for the transition to three-dimensional flow, the drag coefficients obtained from the three-dimensional computations by Henderson (1997), and the experimentally measured drag coefficients from Wieselberger (1921), exhibit a decrease in magnitude from $C_D \approx 1.4$ at $Re \approx 190$ to $C_D \approx 1$ at $Re \approx 1000$. In contrast, the drag coefficients obtained from the two-dimensional computations of the present study and the study by Henderson (1995) increase in magnitude from $C_D \approx 1.4$ at $Re \approx 190$ to $C_D \approx 1.5$ at $Re \approx 1000$.

The pressure and viscous components of the drag coefficient from both steady and unsteady two-dimensional computations were determined by Henderson (1995). He showed that beyond the transition to unsteady flow, the mean pressure component of the drag coefficient increased, whereas the mean viscous component of the drag coefficient decreased. The reduction in the total drag coefficient due to the decrease in the viscous component continued beyond $Re \approx 1 \times 10^2$. For $Re \gtrsim 200$, the total mean drag coefficient increased, as the pressure drag increase outweighed the viscous drag decrease. In figure 5, the computed mean pressure and viscous components of the drag coefficient are presented. These are compared with the reported pressure and viscous components computed by Henderson (1995), which are regarded as reliable. Excellent agreement is obtained, with no perceivable discrepancy between the two sets of predictions in either the steady or unsteady flow regimes.

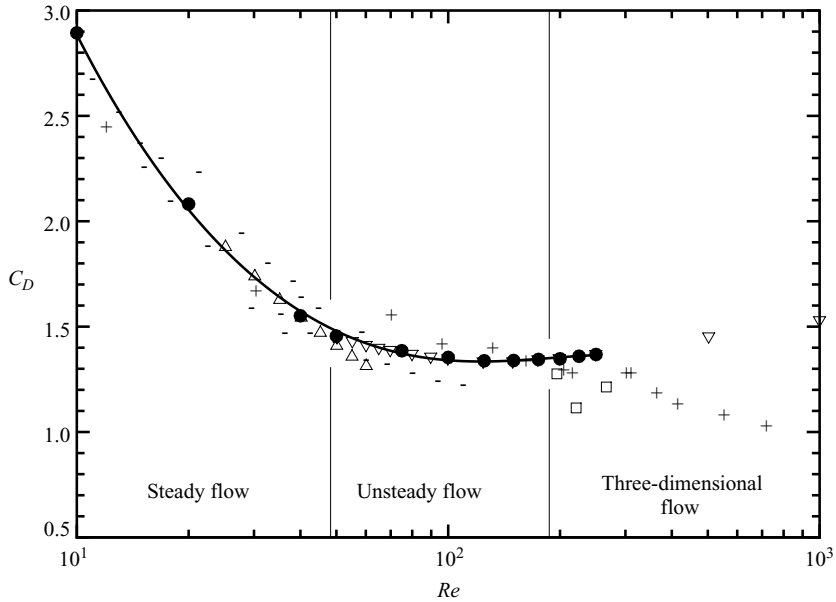


FIGURE 4. A comparison between the computed drag coefficients for the flow past a circular cylinder (solid line and circles) with previously reported values. The steady and mean drag coefficient measurements from the experiments of Wieselberger (1921) are represented by the symbols $-$ and $+$, respectively. The steady and mean drag coefficients from the two-dimensional computations by Henderson (1995) are represented by Δ and ∇ , respectively. The mean drag coefficients from the three-dimensional computations by Henderson (1997) are represented by \square . The vertical lines indicate the Reynolds numbers for the transition from steady to unsteady flow at $Re \approx 47$, and the transition from two- to three-dimensional flow at $Re \approx 189$.

4. Drag coefficients computed for the axisymmetric flow past rings

The drag coefficients for the flow past rings were computed and are analysed here. In figure 6, the computed drag coefficients are compared with the computed drag coefficients for a sphere and a circular cylinder. The figure includes a plot of both C_D versus $\log Re$, and $\log C_D$ versus $\log Re$, for clarity.

The curves presented in figure 6(a) show a significant decrease in C_D with an increase in Reynolds number for all geometries. The decrease in the computed drag coefficients can be attributed to the decrease in the viscous component of the drag as the Reynolds number increases. There is a significant difference between the computed drag coefficient curve for a sphere and for a ring with $A_R \geq 1$. For a ring with $A_R = 1$, the drag coefficient variation is similar in gradient, but is significantly smaller in magnitude than that for a sphere. This can be explained in terms of the choice of length scale used to define the Reynolds number.

For rings, the dimension with which the wake scales varies in a complicated fashion with aspect ratio. This study will present evidence that supports the observations of earlier studies (Lewke & Provansal 1995; Sheard *et al.* 2003, 2004a,b), which show that basing the Reynolds number on the length d is suitable for rings with $A_R \gtrsim 5$ (consistent with studies of the flow past a circular cylinder) and for rings with $A_R \approx 0$ (consistent with studies of the flow past a sphere), but not for rings with aspect ratios between these limits. The intermediate range of aspect ratios $0 < A_R \lesssim 5$ is one in which a significant alteration in wake topology occurs, from wakes which scale on the outer diameter of the ring at smaller aspect ratios, to those which scale on the

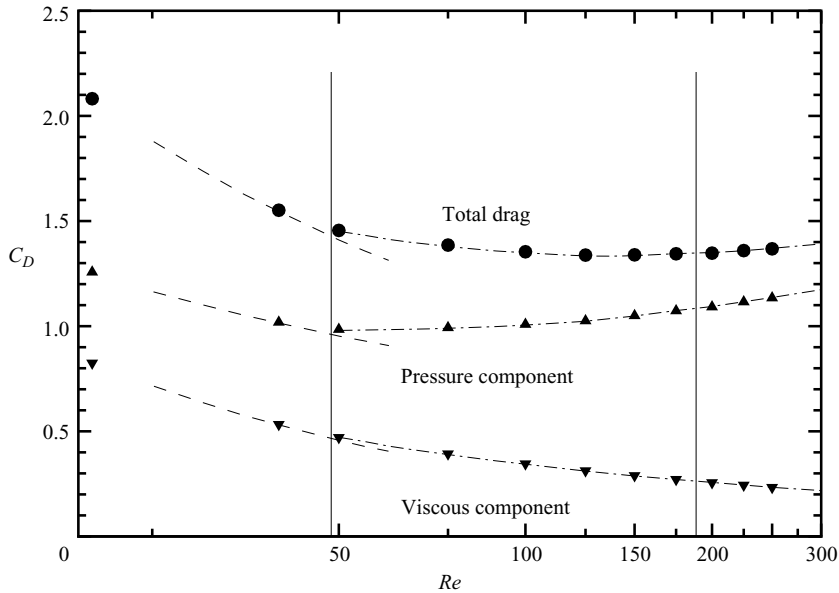


FIGURE 5. A comparison between the present and previous computations of the drag coefficient of the flow past a circular cylinder. Pressure and viscous components of the drag coefficient are also included. The computed drag coefficients, and the pressure and viscous components are represented by ●, ▲ and ▼, respectively. The steady and mean drag coefficients and components computed by Henderson (1995) are represented by dashed and dash-dot lines, respectively. The vertical lines indicate the Reynolds numbers for the transition from steady to unsteady flow at $Re \approx 47$, and the transition from two- to three-dimensional flow at $Re \approx 189$.

Aspect ratio range	Governing length scale L
$A_R = 0$	$L = d$
$0 < A_R \lesssim 2$	$L = D + d$
$2 \rightarrow A_R \rightarrow 5$	$D + d \rightarrow L \rightarrow d$
$A_R \gtrsim 5$	$L \approx d$

TABLE 3. Length dimension on which the wake scales for rings of various aspect ratio.

cross-section of the ring at larger aspect ratios. Details of the structure and stability of the wakes at these aspect ratios lie outside the scope of this paper, but may be found in Sheard *et al.* (2003, 2004a,b). A summary of the variation in effective length scale with aspect ratio is given in table 3.

The Reynolds number for the computations was based on the cross-section diameter, d , and not the projected frontal diameter, $D + d$, which effectively shifts the drag coefficient profiles for rings with $1 \lesssim A_R \lesssim 3$ to the left in figure 6. From the computed results, the drag decreases for a given Reynolds number as the aspect ratio is increased from $A_R = 0$ to $A_R = 1$. The plots in figure 6 include a Reynolds number correction $Re' = Re/2^2$ for the drag coefficient for the flow past a sphere to compensate for the change in length scale between $A_R = 1$ and 0. The correction produces a more uniform progression in the shape of the C_D-Re curves over the range of aspect ratios considered.

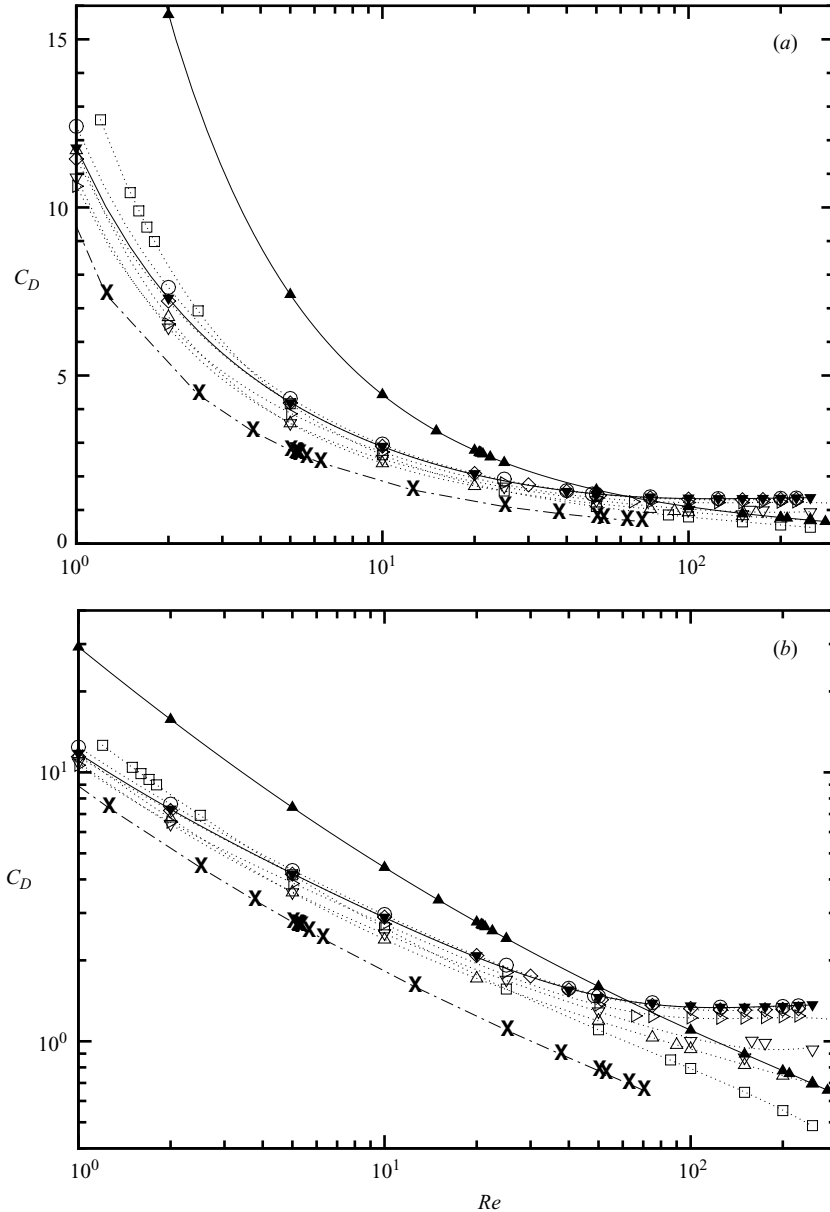


FIGURE 6. Plots of the computed drag coefficients for a sphere, a circular cylinder and rings. (a) C_D against Re with a logarithmic abscissa scale, and (b) C_D against Re with logarithmic abscissa and ordinate scales. For rings, dotted lines are included for guidance, and symbols \square , \triangle , ∇ , \triangleright , \diamond and \circ represent rings with $A_R = 1, 2, 3, 5, 10$ and 20 , respectively. The sphere and circular cylinder, are represented by \blacktriangle and \blacktriangledown , respectively, and solid lines are included for guidance. The dash-dot line and \times symbols represent the drag for a sphere corrected for wake length-scale alteration.

Figure 6 shows that for Reynolds numbers $Re \lesssim 5$, a decrease in the computed drag coefficient is found as the aspect ratio increases from $A_R = 1$ to $A_R \approx 3$, whereas the drag coefficient increases with further increases in aspect ratio. At higher Reynolds numbers ($Re \gtrsim 20$), the computed drag coefficients obtained for $A_R = 1$

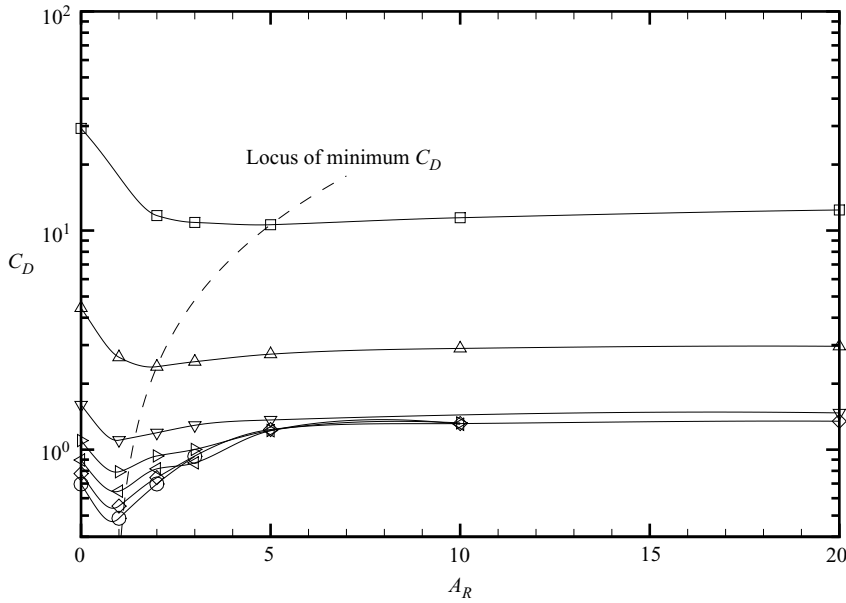


FIGURE 7. C_D against A_R for the flow past rings. Reynolds numbers $Re = 1, 10, 50, 100, 150, 200$ and 250 are represented by $\square, \triangle, \nabla, \triangleright, \triangleleft, \diamond$ and \circ , respectively. Lines are included for guidance, and show the variation in C_D with A_R at a constant Reynolds number. The locus of minimum drag coefficient is indicated by a dashed line.

were the smallest for any aspect ratio included in this study. It can be observed in figure 6(b) that for $Re \gtrsim 20$, the C_D-Re profiles computed for the flow past rings with $A_R > 1$ approach constant values. For $A_R \gtrsim 5$, the computed drag coefficients reach a minimum of $C_D \approx 1.2$. This is interesting, as for unsteady wakes the drag coefficient does not continue to decrease with an increase in Reynolds number; instead it approaches a near-constant value.

To develop a better understanding of the drag coefficient variation with aspect ratio for a given Reynolds number, a plot of C_D against A_R is presented in figure 7, revealing some striking features. As previously discussed, the computed drag coefficients decrease monotonically in magnitude as the Reynolds number is increased. For each Reynolds number, the drag is approximately constant for $A_R \gtrsim 5$. It is pertinent to note that for all Reynolds numbers $Re \gtrsim 50$ over the range of aspect ratios $A_R \gtrsim 5$, the drag coefficients are approximately equal. This corroborates previous observations of the mean drag coefficient measurements of the unsteady flow past a circular cylinder (see figure 4), which showed limited variation in total drag for Reynolds numbers $Re \gtrsim 50$.

An additional feature of interest occurs in the small-aspect-ratio range. For all Reynolds numbers, a minimum in the computed drag coefficient is found in the range $0 < A_R \leq 5$. At $Re = 1$, the minimum drag coefficient occurs for a ring with $A_R = 5$. At $Re = 10$, the minimum drag coefficient occurs for a ring with $A_R = 2$. For all Reynolds numbers $Re \gtrsim 50$, the minimum drag coefficient is found for a ring with $A_R = 1$.

The plot in figure 6(b) shows that the C_D-Re profiles for Reynolds numbers $Re \lesssim 10$ are approximately linear when plotted on logarithmic axes. Using predicted values of $\log C_D$ in the vicinity of $\log Re = 0$, the parameters were determined for a functional

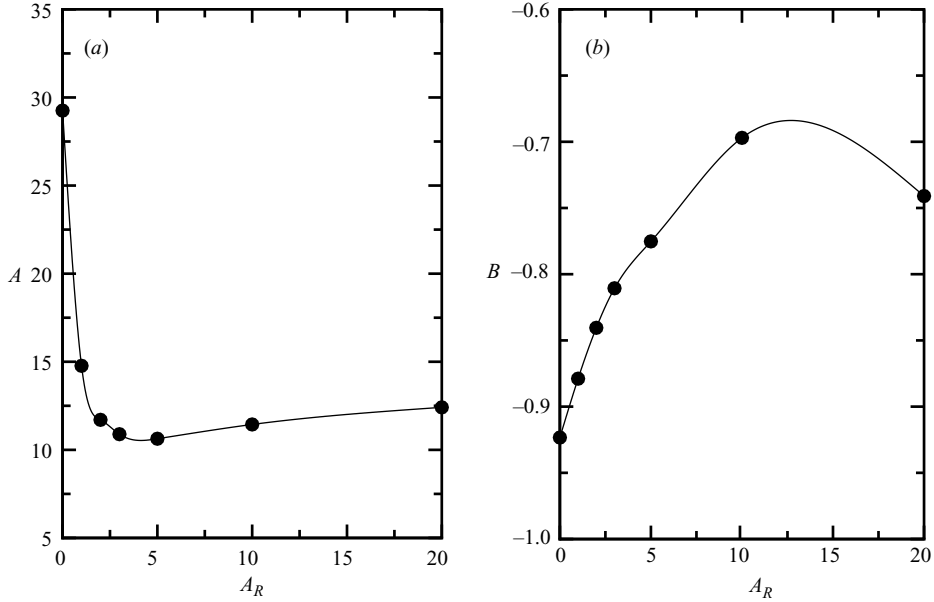


FIGURE 8. The A_R -variation of the coefficients of the functional fit to the low-Reynolds-number C_D data for the flow past rings. The function is of the form $C_D = AR e^B$, and (a) and (b) plot the variation in A and B , respectively. \bullet symbols show the computed coefficients, and the solid lines show cubic spline fits to the data for guidance.

fit to the drag coefficient data in the form

$$C_D \approx AR e^B. \quad (4.1)$$

Figure 8 shows the computed coefficients for the functional fit of the low-Reynolds-number drag coefficients. The Reynolds number exponent lies in the range $-0.93 \lesssim B \lesssim -0.68$, which agrees well with values calculated from existing data (Wieselberger 1921; Proudman & Pearson 1957; Roos & Willmarth 1971; Dennis & Walker 1971; White 1999).

The contribution of the pressure and viscous components to the drag coefficient of a circular cylinder was discussed in §3.2. The contribution of these individual components to the drag coefficients for rings is examined in the following discussion.

The pressure and viscous contributions to the drag coefficients for the flow past rings were calculated, and are plotted in figure 9. Consider first the pressure contribution plotted in figure 9(a). Aside from the C_{D_p} profile of the wake of a sphere (whose large deviation from the ring with $A_R = 1$ due to inappropriate length scaling has already been discussed), all the C_{D_p} profiles exhibit similar behaviour. At Reynolds numbers $Re \approx 4$, the ring with $A_R = 3$ has the lowest pressure drag of the rings considered, with $C_{D_p} \approx 1.9$. At $Re = 4$, the ring with $A_R = 1$ has $C_{D_p} \approx 2.1$, which decreases more rapidly than the pressure drag for the other rings as the Reynolds number is increased. For Reynolds numbers $Re \gtrsim 20$, the profile of the pressure drag is consistent with the profile of that for a sphere. At a Reynolds number of $Re = 250$, the pressure contribution to the drag for both a sphere and a ring with $A_R = 1$ are as low as $C_{D_p} \approx 0.35$. The pressure drag for a ring with $A_R = 2$ varies in a similar fashion, decreasing to $C_{D_p} \approx 0.6$ at $Re = 250$.

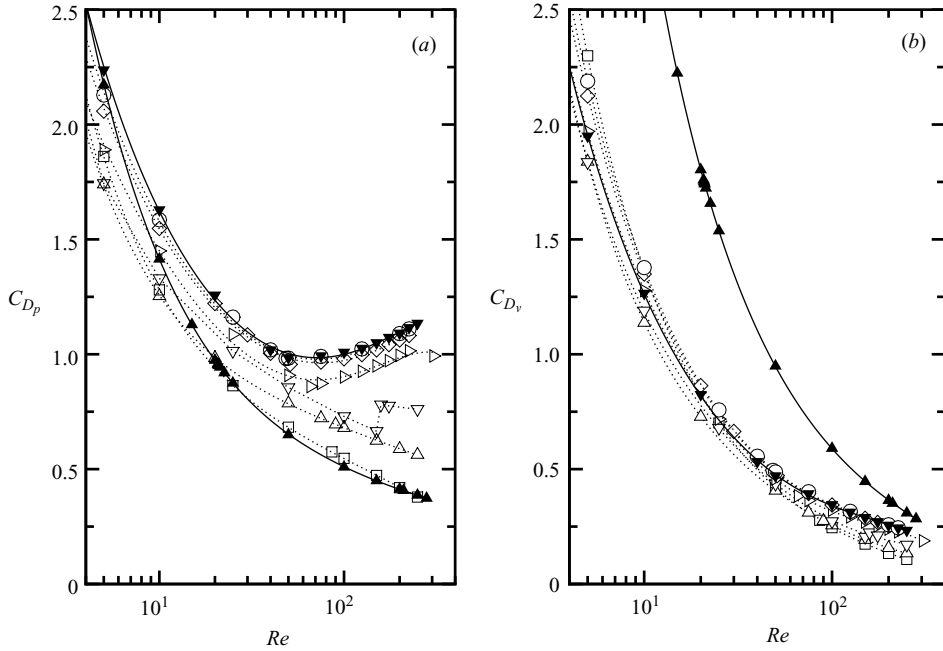


FIGURE 9. (a) Pressure and (b) viscous components of the drag coefficient against Re computed for flows past rings, a sphere, and a circular cylinder. Lines and symbols are as on figure 6.

At $Re=4$, the pressure component for rings with $A_R \geq 5$ varies with an increase in aspect ratio over the range $2.1 \lesssim C_{D_p} \lesssim 2.5$. At $Re \approx 50$, the flows become unsteady, and as in the study of the drag coefficient of the flow past a circular cylinder by Henderson (1995), the pressure component of the drag coefficient reaches a minimum, and then increases with Reynolds number for $Re \geq 50$. Figure 9(a) clearly shows this increase, with the pressure component of the drag coefficients for the flow past rings with $A_R \geq 5$ and a circular cylinder computed between $0.85 \lesssim C_{D_p} \lesssim 1.0$ at $Re \approx 50$, and between $1.0 \lesssim C_{D_p} \lesssim 1.15$ at $Re=200$. For a ring with $A_R=3$, the pressure component increases with Reynolds number beyond $Re \geq 150$. In contrast to the larger aspect ratios discussed previously, the pressure component increase is more pronounced for the ring with $A_R=3$, as it increases from $C_{D_p} \approx 0.7$ at $Re=150$ to $C_{D_p} \approx 0.8$ at $Re \approx 158$.

A plot of the viscous component of the drag coefficients is presented in figure 9(b). A large difference can be observed between the profiles of the viscous component of the drag coefficient for the flows past rings with $A_R=0$ and $A_R=1$, which is due to the wake length scale issue discussed earlier. The minimum viscous component of the drag coefficient is computed for the flow past a ring with $A_R=3$. At $Re=5$, for example, $C_{D_v} \approx 1.8$ for a ring with $A_R=3$, whereas $C_{D_v} \approx 2.3$ for a ring with $A_R=1$ and $C_{D_v} \approx 2.2$ for $A_R=20$. Interestingly, the viscous component of the drag coefficient for a circular cylinder is a little lower for $Re \lesssim 5$, with $C_{D_v} \approx 2.0$. The probable explanation for this discrepancy is the difference between the formulation of the axisymmetric and two-dimensional models for rings and circular cylinders. Recall that the computational model for the circular cylinder comprised free-stream velocity boundaries $30d$ from the cylinder in the transverse direction, whereas the ring was modelled with a free-stream velocity boundary at a radial distance of $30d$ from the

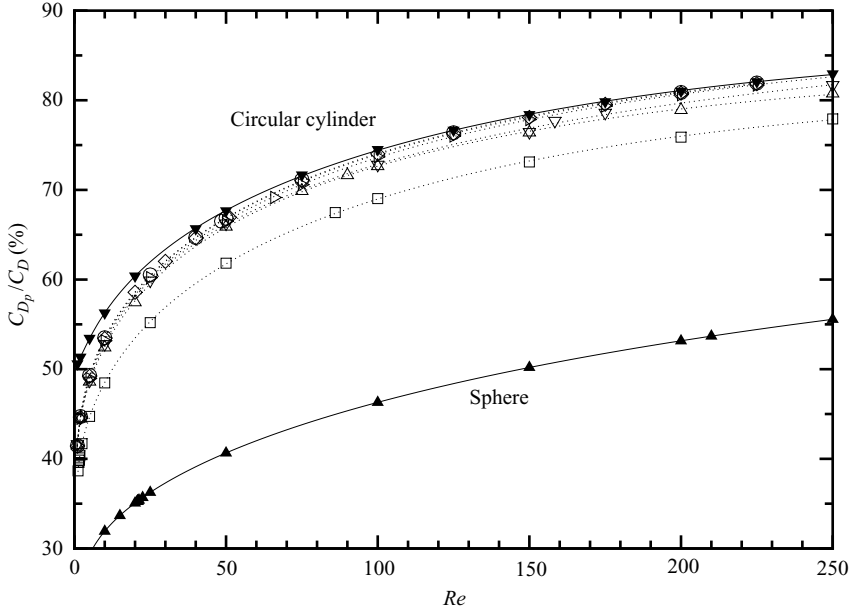


FIGURE 10. The percentage contribution of C_{D_p} to C_D against Re for the flow past rings, a sphere, and a circular cylinder. Lines and symbols are as on figure 6.

ring, and a zero-normal-velocity boundary at the axis of symmetry ($r=0$). Clearly, at low Reynolds numbers blockage has a greater effect, resulting in the discrepancy. At higher Reynolds numbers the flow past the ring is much less sensitive to the presence of the computational boundaries (i.e. see figure 9(b), where the viscous component of the drag for a circular cylinder and a ring with $A_R=20$ align more closely).

An alternative representation of the contributions of pressure and viscous stress to the total drag is presented in figure 10. This shows the percentage contribution of the pressure component to the total drag coefficient as a function of Reynolds number for each of the aspect ratios considered.

Two important points should be drawn from figure 10. First, the pressure drag component percentages for all rings vary in a manner similar to those computed for both a sphere and a circular cylinder. Secondly, the magnitude of the percentage contribution at any given Reynolds number increases with aspect ratio. The minimum percentage contribution of the pressure component occurs for a sphere, and the maximum percentage contribution occurs for a circular cylinder.

5. Drag coefficients computed for the non-axisymmetric flow past rings

In this section, the effect of the development of non-axisymmetric instabilities on the drag coefficient is investigated for time-dependent flow. The previous studies of the drag coefficient of a sphere have shown that little variation is observed after the transition to non-axisymmetric flow (see figure 3), whereas for a circular cylinder a sudden reduction is observed in the drag coefficient after the transition to three-dimensional flow. Drag coefficients were therefore computed for the non-axisymmetric flow past rings with $A_R=5, 10$ and 20 , to determine the variation in the drag coefficient caused by transition to three-dimensional flow.

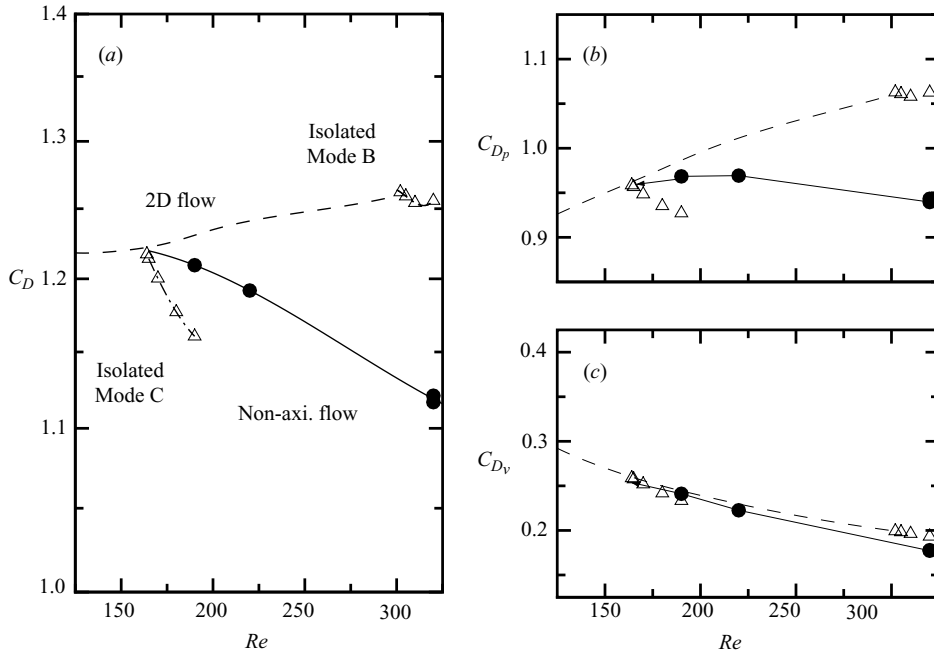


FIGURE 11. The drag coefficient variation against Reynolds number for the non-axisymmetric flow past a ring with $A_R = 5$. The C_D , C_{D_p} and C_{D_v} variations with Re are plotted in (a), (b) and (c), respectively. The dotted line shows the coefficients calculated from axisymmetric computations, Δ shows the coefficients calculated from non-axisymmetric computations from Sheard *et al.* (2004b) which isolated the pure instabilities, \bullet shows the coefficients calculated from non-axisymmetric computations with a larger azimuthal domain size, and the solid line is included for guidance.

For these aspect ratios, the transition to non-axisymmetric flow occurs through the amplification of instabilities known as Modes A, B and C (Williamson 1988b, 1996a, b; Sheard *et al.* 2003, 2004b). Of these, only Modes A and B are observed in the wake behind a circular cylinder. Importantly, with variation in aspect ratio the order in which these instabilities occurs changes. For $A_R = 5$ the first-occurring instability is Mode C, whereas for $A_R = 10$ and $A_R = 20$ the first-occurring instability is Mode A. The Mode C and Mode A instabilities differ in terms of their spatio-temporal symmetry (Mode C is subharmonic, Mode A is not), azimuthal wavelength (Mode C is approximately $1.7d$ in wavelength, whereas Mode A is approximately $4d$), and crucial to this study, Mode C is supercritical whereas Mode A is not. Put simply, a ring with $A_R = 5$ undergoes a continuous bifurcation to non-axisymmetric flow through the development of a Mode C instability, whereas rings with $A_R = 10$ and 20 undergo a discontinuous bifurcation through the development of a Mode A instability.

The plots to follow include computed drag coefficients in which one non-axisymmetric instability was isolated in the flow, as well as coefficients from exhaustive computations with an azimuthal domain sufficiently large to allow competition between the instabilities. Pure modes were isolated by limiting the azimuthal domain size so that only the shortest-wavelength unstable mode could grow (i.e. approximately $4d$ for Mode A, $1.6d$ for Mode C and $0.8d$ for Mode B). For the computations used to capture multiple instability modes, azimuthal domains giving a distance along the ring span of approximately $4d$ and $8d$ were used. The small but perceptible discrepancy between the pair of points at $Re = 320$ on the non-axisymmetric C_D curve in figure 11

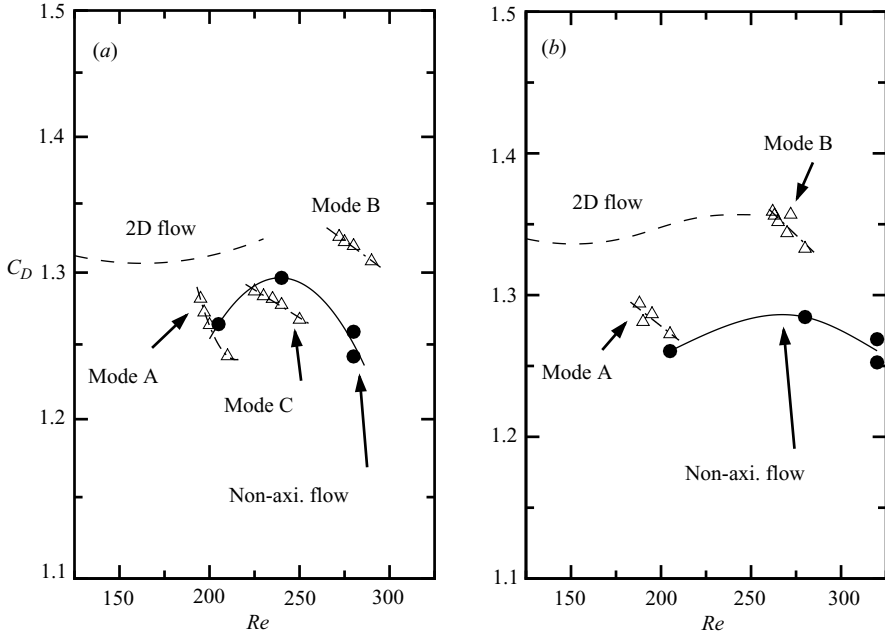


FIGURE 12. The drag coefficient variation against Reynolds number for the non-axisymmetric flows past rings with $A_R = 10$ (a) and $A_R = 20$ (b). Lines and symbols are as on figure 11.

is a product of the relatively short duration over which data could be collected due to the computational expense of the simulations.

In figure 11, plots are presented which show the Reynolds number variation of C_D , and the pressure and viscous components C_{D_p} and C_{D_v} , for a ring with $A_R = 5$. In these plots, the drag coefficient profile that was obtained for axisymmetric computations is also included. The data from the full non-axisymmetric computations are distinguished from the data in which a single mode was isolated by the use of solid guidance lines. Importantly, with an increase in Reynolds number, the drag coefficient for non-axisymmetric flow decreases. This is in agreement with the observed behaviour for three-dimensional flow in the wake of a circular cylinder (see figure 4). The bifurcation of the drag coefficient from the axisymmetric profile appears to be continuous. This verifies the prediction from Sheard *et al.* (2004b), who showed that the transition to non-axisymmetric flow for a ring with $A_R = 5$ occurred through a continuous supercritical bifurcation to Mode C.

The plots presented in figure 11(b,c) show that the decrease in the drag coefficient with increasing Reynolds number occurs due to a reduction in the pressure component through the transition from axisymmetric to non-axisymmetric flow. Interestingly, the transition to non-axisymmetric flow has almost no influence on the viscous drag, as shown in figure 11(c).

In figure 12 plots of the variation in drag coefficient with Reynolds number for $A_R = 10$ and $A_R = 20$ are presented. These plots show that the drag coefficients obtained from non-axisymmetric computations at a given Reynolds number are about 7% smaller than the drag coefficients obtained with imposed axisymmetry. Interestingly, the plots indicate that at the onset of non-axisymmetric flow, a discontinuous reduction in the drag coefficient is obtained. This observation is consistent with the computations of Sheard *et al.* (2004b), which showed that the initial non-axisymmetric

transition for rings with $A_R = 10$ and $A_R = 20$ occurs through a discontinuous sub-critical bifurcation to Mode A.

6. Conclusions

Axisymmetric and two-dimensional computations have verified that the drag coefficients for the flows past a sphere and a circular cylinder are accurately determined when the present numerical scheme and meshes are employed.

Axisymmetric computations of the flow past rings have provided the drag coefficients over a range of Reynolds numbers $1 \leq Re \lesssim 300$, and a range of aspect ratios $0 \leq A_R \leq 20$. The computed drag coefficients show that with a decrease in Reynolds number, the aspect ratio with the minimum drag coefficient increases from $A_R = 1$ at $Re \approx 50$ to $A_R = 5$ at $Re = 1$, and presumably $A_R \rightarrow \infty$ as $Re \rightarrow 0$. Least-squares power-law fits to the low-Reynolds-number drag coefficients for rings have been established. For the range $Re \lesssim 100$, these fits are accurate to 2%.

The variation in drag coefficient over the aspect ratio range $0 < A_R \lesssim 5$ is consistent with previous suggestions that the wake does not scale on the minor ring dimension d in this range. A modified length scale used in the determination of Reynolds number for a ring with $A_R = 0$ markedly improves the uniformity in C_D - Re trends for rings.

Non-axisymmetric computations have provided the drag coefficient variation for rings at $A_R = 5, 10$ and 20 . The onset of time-dependent non-axisymmetric flow is shown to cause a substantial reduction in the drag coefficient. In both the axisymmetric and non-axisymmetric computations the variation in the drag coefficient as the flow undergoes a variety of transitions is shown to occur predominantly through variation in the pressure component of the drag coefficient. The viscous component of the drag coefficient decreases with an increase in Reynolds number throughout the various flow regimes.

In summary, previous work has shown that a rich variety of transitions and flow states occur for low-Reynolds-number flows past rings. This study complements these previous studies by documenting the quantitative variation of the drag as a function of Reynolds number and aspect ratio as the flow undergoes these transitions.

The authors wish to thank the Victorian Partnership for Advanced Computing (VPAC) consortium for access to the computational resources necessary to complete this study. This paper was supported by an ARC Linkage International Grant. G. J. S. received some financial assistance from a Monash University Postgraduate Publication Award.

REFERENCES

- ACHENBACH, E. 1974 Vortex shedding from spheres. *J. Fluid Mech.* **62**, 209–221.
- BARKLEY, D. & HENDERSON, R. D. 1996 Three-dimensional Floquet stability analysis of the wake of a circular cylinder. *J. Fluid Mech.* **322**, 215–241.
- BEARMAN, P. W. & TAKAMOTO, M. 1988 Vortex shedding behind rings and discs. *Fluid Dyn. Res.* **3**, 214–218.
- BLACKBURN, H. M. & HENDERSON, R. 1994 Body-wake interaction during vortex-induced vibration. In *Proc. Intl Colloquium on Jets, Wakes and Shear Layers* (ed. K. Hourigan). CSIRO, Melbourne, Australia.
- BLACKBURN, H. M. & HENDERSON, R. 1996 Lock-in behavior in simulated vortex-induced vibration. *Expl Therm. Fluid Sci.* **12**, 184–189.
- CLIFT, R., GRACE, J. R. & WEBER, M. E. 1978 *Bubbles, Drops and Particles*. Academic.

- DENNIS, S. C. R. & WALKER, J. D. A. 1971 Calculation of the steady flow past a sphere at low and moderate Reynolds numbers. *J. Fluid Mech.* **48**, 771–789.
- DUŠEK, J., LE GAL, P. & FRAUNÉ, P. 1994 A numerical and theoretical study of the first Hopf bifurcation in a cylinder wake. *J. Fluid Mech.* **264**, 59–80.
- GHIDERSA, B. & DUŠEK, J. 2000 Breaking of axisymmetry and onset of unsteadiness in the wake of a sphere. *J. Fluid Mech.* **423**, 33–69.
- GOREN, S. L. & O'NEILL, M. E. 1980 Asymmetric creeping motion of an open torus. *J. Fluid Mech.* **101**, 97–110.
- HENDERSON, R. D. 1995 Details of the drag curve near the onset of vortex shedding. *Phys. Fluids* **7**, 2102–2104.
- HENDERSON, R. D. 1997 Non-linear dynamics and pattern formation in turbulent wake transition. *J. Fluid Mech.* **352**, 65–112.
- JENNY, M., DUŠEK, J. & BOUCHET, G. 2004 Instabilities and transition of a sphere falling or ascending freely in a Newtonian fluid. *J. Fluid Mech.* **508**, 201–239.
- JOHNSON, R. E. & WU, T. Y. 1979 Hydromechanics of low-Reynolds number flow. Part 5. motion of a slender torus. *J. Fluid Mech.* **95**, 263–277.
- JOHNSON, T. A. & PATEL, V. C. 1999 Flow past a sphere up to a Reynolds number of 300. *J. Fluid Mech.* **378**, 19–70.
- LEWEKE, T. & PROVANSAL, M. 1995 The flow behind rings: Bluff body wakes without end effects. *J. Fluid Mech.* **288**, 265–310.
- MITTAL, R. 1999 A Fourier-Chebyshev spectral collocation method for simulating flow past spheres and spheroids. *Intl J. Numer. Meth. Fluids* **30**, 921–937.
- MONSON, D. R. 1983 The effect of transverse curvature on the drag and vortex shedding of elongated bluff bodies at low Reynolds number. *Trans. ASME I: J. Fluids Engng* **105**, 308–317.
- NATARAJAN, R. & ACRIVOS, A. 1993 The instability of the steady flow past spheres and disks. *J. Fluid Mech.* **254**, 323–344.
- NOACK, B. R. & ECKELMANN, H. 1994 A low-dimensional Galerkin method for the three-dimensional flow around a circular cylinder. *Phys. Fluids* **6**, 124–143.
- NORBERG, C. 1994 An experimental investigation of the flow around a circular cylinder: Influence of aspect ratio. *J. Fluid Mech.* **258**, 287–316.
- PATERA, A. T. 1984 A spectral element method for fluid dynamics: Laminar flow in a channel expansion. *J. Comput. Phys.* **54**, 468–488.
- PROUDMAN, I. & PEARSON, J. R. A. 1957 Expansions at small Reynolds numbers for the flow past a sphere and a circular cylinder. *J. Fluid Mech.* **2**, 237–262.
- PROVANSAL, M., MATHIS, C. & BOYER, L. 1987 Bénard-von Kármán instability: Transient and forced regimes. *J. Fluid Mech.* **182**, 1–22.
- ROOS, F. W. & WILLMARTH, W. W. 1971 Some experimental results on sphere and disk drag. *AIAA J.* **9**, 285–291.
- ROSHKO, A. 1954 On the development of turbulent wakes from vortex streets. *NACA Rep.* 1191, pp. 1–25.
- SHEARD, G. J. 2004 The stability and characteristics of the flow past rings. PhD thesis, Monash University, Melbourne, Australia.
- SHEARD, G. J., THOMPSON, M. C. & HOURIGAN, K. 2003 From spheres to circular cylinders: The stability and flow structures of bluff ring wakes. *J. Fluid Mech.* **492**, 147–180.
- SHEARD, G. J., THOMPSON, M. C. & HOURIGAN, K. 2004a Asymmetric structure and non-linear transition behaviour of the wakes of toroidal bodies. *Euro. J. Mech. B (Fluids)* **23**, 167–179.
- SHEARD, G. J., THOMPSON, M. C. & HOURIGAN, K. 2004b From spheres to circular cylinders: Non-axisymmetric transitions in the flow past rings. *J. Fluid Mech.* **506**, 45–78.
- TANEDA, S. 1956a Experimental investigation of the wake behind a sphere at low Reynolds numbers. *J. Phys. Soc. Japan* **11**, 1104–1108.
- TANEDA, S. 1956b Experimental investigation of the wakes behind cylinders and plates at low Reynolds numbers. *J. Phys. Soc. Japan* **11**, 302–307.
- THOMPSON, M. C., HOURIGAN, K. & SHERIDAN, J. 1994 Three-dimensional instabilities in the wake of a circular cylinder. In *Proc. Intl Colloquium on Jets, Wakes and Shear Layers* (ed. K. Hourigan). CSIRO, Melbourne, Australia.
- THOMPSON, M. C., HOURIGAN, K. & SHERIDAN, J. 1996 Three-dimensional instabilities in the wake of a circular cylinder. *Expl Therm. Fluid Sci.* **12**, 190–196.

- THOMPSON, M. C., LEWEKE, T. & PROVANSAL, M. 2001 Kinematics and dynamics of sphere wake transition. *J. Fluids Struct.* **15**, 575–585.
- TOMBOULIDES, A. G. & ORSZAG, S. A. 2000 Numerical investigation of transitional and weak turbulent flow past a sphere. *J. Fluid Mech.* **416**, 45–73.
- TOMBOULIDES, A. G., ORSZAG, S. A. & KARNIADAKIS, G. E. 1993 Direct and large-eddy simulation of the flow past a sphere. In *Proc. Second Intl Conf. on Turbulence Modeling and Experiments (2nd ICTME)*, Florence, Italy.
- WHITE, F. M. 1999 *Fluid Mechanics: Fourth Edition*. WBC/McGraw-Hill.
- WIESELBERGER, C. 1921 Neuere feststellungen über die Gestze des Flüssigkeits- und Luftwiderstands. *Phys. Z.* **22**, 321–328.
- WILLIAMSON, C. H. K. 1988a Defining a universal and continuous Strouhal-Reynolds number relationship for the laminar vortex shedding of a circular cylinder. *Phys. Fluids* **31**, 2742–2744.
- WILLIAMSON, C. H. K. 1988b The existence of two stages in the transition to three-dimensionality of a cylinder wake. *Phys. Fluids* **31**, 3165–3168.
- WILLIAMSON, C. H. K. 1989 Oblique and parallel mode of vortex shedding in the wake of a circular cylinder at low Reynolds numbers. *J. Fluid Mech.* **206**, 579–627.
- WILLIAMSON, C. H. K. 1992 The natural and forced formation of spot-like ‘vortex dislocations’ in the transition of a wake. *J. Fluid Mech.* **243**, 393–441.
- WILLIAMSON, C. H. K. 1996a Mode A secondary instability in wake transition. *Phys. Fluids* **8**, 1680–1682.
- WILLIAMSON, C. H. K. 1996b Three-dimensional wake transition. *J. Fluid Mech.* **328**, 345–407.
- WILLIAMSON, C. H. K. 1996c Vortex dynamics in the cylinder wake. *Annu. Rev. Fluid Mech.* **28**, 477–539.
- WILLIAMSON, C. H. K. & ROSHKO, A. 1990 Measurements of base pressure in the wake of a cylinder at low Reynolds number. *Z. Flugwiss. Weltraumforsch.* **14**, 38–46.